Dynamic Virtual Power Plant Design for Fast Frequency Reserves: Coordinating Hydro and Wind

Joakim Björk , *Member, IEEE*, Karl Henrik Johansson , *Fellow, IEEE*, and Florian Dörfler , *Senior Member, IEEE*

Abstract—To ensure frequency stability in future low-inertia power grids, fast ancillary services, such as fast frequency reserves (FFR), have been proposed. In this work, the coordination of conventional (slow) frequency containment reserves (FCR) with FFR is treated as a decentralized model-matching problem. The design results in a dynamic virtual power plant (DVPP), whose aggregated output fulfills the system operator's (SO's) requirements in all timescales, while accounting for the capacity and bandwidth limitation of participating devices. This is illustrated in a 5-machine representation of the Nordic synchronous grid. In the Nordic grid, stability issues and bandwidth limitations associated with nonminimum phase zeros of hydropower is a well-known problem. By simulating the disconnection of a 1400 MW importing dc link, it is shown that the proposed DVPP design allows for coordinating fast FFR from wind, with slow FCR from hydro, while respecting dynamic limitations of all participating devices. The SO's requirements are fulfilled in a realistic low-inertia scenario without the need to install battery storage or to waste wind energy by curtailing the wind turbines.

Index Terms—Decentralized control, frequency stability, low-inertia power systems, model-matching, nonminimum phase, smart grid.

I. INTRODUCTION

DEREGULATION of the market and the transition toward renewable energy is diversifying the mechanics behind

electricity production. Regulatory services provided by distributed energy resources coordinated as virtual plants are expected to be an important supplement to the services provided by large-scale power plants [1]. At the same time, the frequency stability of grids is becoming more sensitive to load imbalances due to the growing share of converter-interfaced generation [2]. A number of recent blackouts are related to large frequency disturbances. The incidence of this phenomenon is expected to increase in the future as the energy transition continues; in fact, they have doubled from the early 2000s [3]. With growing shares of renewables, system operators (SOs) are therefore increasingly demanding renewable generation and other small-scale producers to participate in frequency containment reserves (FCR) [4].

Virtual power plants (VPPs), aggregating together groups of small-scale producers and consumers, is a proposed solution to allow smaller players with more variable production to enter into the market with the functionality of a larger conventional power plant [1], [5], [6]. The main objectives are to coordinate dispatch, maximize the revenue, and to reduce the financial risk of variable generation, in the day-ahead and intraday markets [7], [8]. However, also other functions, such as voltage regulation [9] and allocation of FCR resources [10]–[12], have been proposed.

In this work, we design controllers that coordinate FCR over all time-scales, beyond mere setpoint tracking, forming a dynamic virtual power plant (DVPP) that offers dynamic ancillary services [13]. While none of the individual devices may be able to provide FCR consistently across all power and energy levels or over all time-scales, a sufficiently heterogeneous and properly coordinated ensemble will be able to do so. An example of heterogeneous devices complementing each other while providing fast frequency reserves (FFR) is shown in [14], where hydropower with initially inverse response dynamics is compensated by battery sources on short time-scales. Power can also be controlled using demand response [15]. In [16], a hybrid energy storage system is designed to even-out the variable production of a wind farm. Supercapacitors are tuned to balance out faster fluctuations, leaving slower disturbances to be absorbed by a flow battery. A stand-alone energy storage system supplied by photovoltaics is proposed in [17]. Combining batteries and supercapacitors, the system is able to supply continuous energy and large bursts of current to a load. In [18]–[20], wind turbines (WTs) are controlled to support the grid with FFR.

WTs operating at the maximum power point (MPP) can provide a quick response but are subject to a rebound effect that has to be compensated by other sources later on [18], [19]. One way to avoid the rebound effect is to operate below the MPP, leaving headroom for the WTs to participate in both FFR and FCR [20].

A drawback of the aforementioned coordination methods is that they are highly customized and not directly extendable to other device aggregations. Furthermore, the methods do not consider the dynamic FCR requirements on a system level. As a result, the aggregate control reserve might have to be overdimensioned. To show how an ensemble of devices can be coordinated to match the system-level requirements, this work considers frequency containment in a model of the Nordic synchronous grid. The proposed method can be used to complement legacy equipment (e.g. a hydro plant) so that it can participate in ancillary grid services.

In the Nordic grid, FCR is almost exclusively provided by hydropower. The controllability and storage capability of hydropower make it ideal for this purpose. In recent years, however, the inertia reduction due to the renewable energy transition has made the bandwidth limitations associated with nonminimum phase (NMP) waterway dynamics a problem. Since the bandwidth of hydro-FCR cannot be increased without reducing the closed-loop stability margins [21], the Nordic SOs have developed a new market for FFR [22]. Units participating in FFR are subjected to ramp down limits and a 10-s buffer period before the device is allowed to recover energy exerted during the FFR event. This helps to avoid a secondary frequency dip before the hydro-FCR has fully activated. However, the requirement of a recovery-period disqualifies the use of uncurtailed WTs. Since these operate at the MPP, any temporary power outtake will decelerate the turbine, thereby immediately lowering the sustainable power output. The open-loop control method proposed in [22] is therefore a potentially costly solution that requires controllable storage devices, such as batteries or curtailing of WTs in order to guarantee the needed FFR capacity.

The contribution of this work is the design of a closed-loop decentralized dynamic ancillary service, distributing FCR and FFR between a heterogeneous ensemble of devices to form a DVPP. The controllers rely on dynamic participation factors (DPFs) and are designed so that all devices collectively match the Bode diagram of a design target, specified by the SO's requirements. Typically, the design target will take the form of a low-pass filter that matches the desired steady-state FCR, but also models the allowed roll-off at higher frequencies. The frequency-dependent DPFs allows us to conveniently allocate the resources in a smart grid with many controllable actuators, and to account for the capacity and speed limitation of each device.

To validate our solution, we first design a DVPP made up of two hydrounits and a battery storage. The FFR from the battery storage complements the response of the hydrounits so that their combined output matches the design target. It is assumed that the battery can be controlled with a sufficiently high bandwidth and has enough storage capacity so that it can match the design target over all time-scales, compensating for the hydrounits when needed. The key strength of our proposed method, however, is that it also allows us to coordinate heterogeneous devices to fulfill the design target even if none of the individual devices can match the design target. This is demonstrated by designing a DVPP where the hydrounits are supplemented with FFR from a wind farm. It is shown that the design can improve the frequency stability of a low-inertia power system using a model of the Nordic synchronous grid. In our case study, the dynamic FCR requirements are met exactly without overly aggressive or overshooting actuation. Hence, the participating devices need not to be oversized in terms of capacity or response time. The design allows us to systematically coordinate devices with different dynamic constraints and time constants. By matching the design target, we provide appropriate compensation for undesirable dynamic properties such as the NMP response of hydrounits or the rebound effect of WTs. The linear design also makes it transparent how each device affects the stability margin of the closed-loop system. The case study shows that the Nordic FCR requirements can be met, even in a low-inertia operating condition, without adding extra battery storage. Finally, we demonstrate the performance of the proposed DVPP design in comparison to a conventional FCR and FFR control designs.

The rest of this article is organized as follows. Section II presents the control problem, introducing the test system and models of controllable energy sources. Section III formally introduces the DVPP control design. In Section IV, a local DVPP is designed, and in Section V, we close the frequency loop and coordinate FCR and FFR in the whole grid. Finally, Section VI concludes this article.

II. PROBLEM FORMULATION

In this work, we are interested in the frequency containment and postfault dynamics of the center of inertia (COI). That is, we do not directly address short term synchronization and interarea oscillations in the control design. In the end, stability is verified in simulations by applying the control to a detailed power system model designed for large signal analysis.

Power balance between production and consumption is ensured by controlling the COI frequency [23]. For a network with n_{gen} synchronous machines, the COI frequency is

$$\omega_{COI} = \frac{\sum_{i=1}^{n_{gen}} M_i \omega_i}{M}, \quad M = \sum_{i=1}^{n_{gen}} M_i$$

where ω_i is the speed and M_i the inertia of machine i. Let $W_{kin,i}$ be the kinetic energy that machine i has stored at nominal frequency f_{nom} (typically 50 or 60 HZ), and then the inertia $M_i = 2W_{kin,i}/f_{nom}$. Assuming that the grid stays connected, the motion of the COI frequency is determined by the power balance

$$sM\omega_{COI} = P_{COI} = \sum_{i=1}^{n} P_{in,i} - P_{out,i}$$

of the n inputs and outputs distributed all over the system.

For the analysis, we assume that physical frequency-dependent or frequency-controlled power sources can be linearized, e.g., neglecting effects of saturation. The power
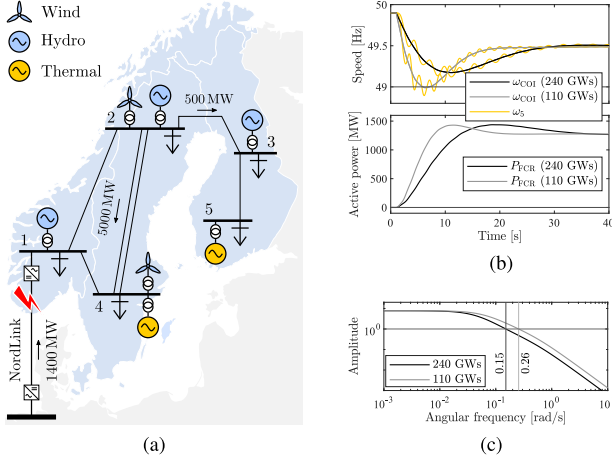
Fig. 1. N5 test system. The full model, and test cases presented in this work, are available at the repository https://github.com/joakimbjork/Nordic5. (a) One-line diagram. (b) Ideal FCR response. (c) Bode diagram of the FCR open-loop.

TABLE I
KINETIC ENERGY W_{KIN} AND PREFAULT POWER INJECTIONS P_e FOR THE 240- AND 110-GWs TEST CASES

Bus	W_{kin} (GWs)	P_e (MW)	W_{kin} (GWs)	P_e (MW)
1	67.5	18 000	34	9000
2	45	12 000	22.5	6000
3	7.5	2000	7.5	2000
4	73.3	11 000	33	5000
5	46.7	7000	13	2000
Σ	240		110	

balance P_{COI} is divided into frequency-dependent power sources $-F_i(s)\omega_{\text{COI}}$ and exogenous[1] power sources or loads u_i, so that

$$P_{\text{COI}} = \sum_{i=1}^{n} u_i - F_i(s)\omega_{\text{COI}} = u - F(s)\omega_{\text{COI}}.$$

We can then express the COI frequency disturbance response

$$\omega_{\text{COI}} = \frac{1}{sM + F(s)} u. \qquad (1)$$

Let $F_i(s)$ be broken up into $F_i(s) = D_i(s) + H_i(s) \cdot K_i(s)$, where $D_i(s)$ is some fixed frequency-dependent load or power source (typically assumed to be a constant), $H_i(s)$ represents the dynamics of some controllable power source, and $K_i(s)$ is a linear FCR controller taking a measurement of the local frequency as input. The goal is then to design $K_i(s)$, $i \in \{1, \ldots, n\}$, so that (1) fulfills the FCR requirements of the SO. In this article, we will study this problem using a case study of a 5-machine representation of the Nordic synchronous grid.

A. Nordic 5-Machine Test System

Consider the Nordic 5-machine (N5) test system shown in Fig. 1(a). The system is phenomenological but has dynamical properties similar to the Nordic synchronous grid. The model is adapted from the empirically validated 3-machine model presented in [24]. Loads, synchronous machines, and WTs are lumped up into a single large unit at each bus. The model is developed in Simulink Simscape Electrical [25]. Hydro and thermal units are modeled as 16th-order salient-pole and round rotor machines, respectively. Assuming that inverters are operated within allowed limits and are fast enough so that their dynamics have only a marginal effect on (1), we model all inverter sources as grid-following controllable power loads.

The amount of synchronous generation connected to the grid varies with the load demand and dispatch. Therefore, the amount of system kinetic energy varies greatly over the year [22]. Here, we will consider a high-inertia scenario, adapted from [24], with total kinetic energy $W_{\text{kin}} = 240$ GWs and a low-inertia scenario with $W_{\text{kin}} = 110$ GWs distributed according to Table I. Loads are modeled as constant power loads with a combined proportional frequency dependency $D(s) = D = 400$ MW/Hz.

To specify a desired "ideal" FCR response, we use the FCR for disturbance (FCR-D) specifications in the Nordic synchronous grid. The FCR-D is used to contain the frequency outside normal operation. Following a rapid frequency fall from 49.9 to 49.5 Hz, the reserves should be 50% activated within 5 s and fully activated in 30 s. Following larger disturbances, the nadir should be limited to 1.0 Hz [26]. Hence, we let the FCR-D design target take the form

$$F_{\text{FCR}}(s) = R_{\text{FCR}} \frac{6.5\,s + 1}{(2\,s + 1)(17\,s + 1)}. \qquad (2)$$

Consider the dimensioning fault to be the instant disconnection of the NordLink dc cable [27] importing 1400 MW from Germany into Norway, as shown in Fig. 1(a). Choosing $R_{\text{FCR}} = 3100$ MW/Hz, the postfault system stabilizes at 49.5 Hz, as seen in Fig. 1(b). The second-order filter in (2) is tuned so that the FCR-D requirements are fulfilled for both scenarios, while also avoiding an overshoot and a second frequency dip when the frequency is restored. For a description of how the FCR-D design target can be selected, see Appendix A.

In Fig. 1(b) and (c), we consider ideal actuation $H_i(s) = 1$. Thus, (2) is realized with ideal controllable power sources distributed at buses 1, 2, and 3 so that the total controlled input $P_{\text{FCR}} = F_{\text{FCR}}(s)(\omega_{\text{ref}} - \hat{\omega})$, where ω_{ref} is the frequency reference and $\hat{\omega} \approx \omega_{\text{COI}}$ is the locally measured frequency. As shown in Fig. 1(b), this approximation has no big impact on the result, assuming that the postfault system remains stable. With reduced inertia, the speed of the system increases. This also increases the cross-over frequency of the FCR open-loop

$$L(s) = F_{\text{FCR}}(s) \frac{1}{sM + D}$$

obtained by breaking the loop at the input/output of $F_{\text{FCR}}(s)$, as shown in Fig. 2. Since real actuators will have bandwidth limitations, the low-inertia scenario therefore poses a greater control challenge.

When deviating from the above ideal actuation scenario, as we will see, the NMP characteristics of hydrounits will make it impossible to match the design target (2). The target can be

---

[1]Exogenous inputs do not depend on the system state (i.e., the local bus frequency). These will therefore not affect the linear stability of the system.
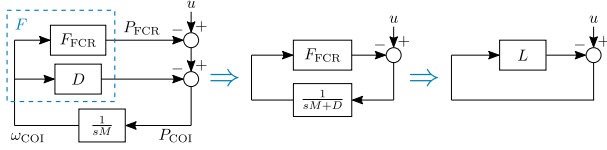
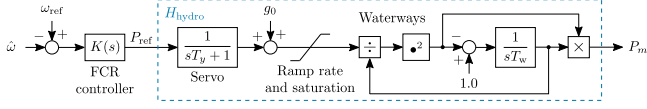Fig. 2. Block diagram of the FCR control loop.

Fig. 3. Block diagram of the hydroturbine and governor model.

modified, by increasing the cross-over frequency, so that the FCR-D requirements are fulfilled even if FCR are delivered by hydro governors. However, due to bandwidth limitations imposed by the NMP zeros (see next section for details), this is not a good solution since this reduces the closed-loop stability margins [21]. Because of this, the Nordic SOs have developed a new market for FFR [22]. FFR can be provided by, e.g., battery sources or wind farms bidding on such a market.

In this work, we consider the control problem of coordinating multiple heterogeneous plants with different time constants and limitations. We will consider hydrounits, batteries, and WTs.

B. Hydro Governor Model

The hydro governor model implemented in this work is an adaption of the hydro governor model available in the Simulink Simscape Electrical library [25]; modified to allow a general linear FCR controller, $K(s)$, instead of the predefined PID/droop control structure, as shown in Fig. 3. The nonlinear second-order model is useful for large-signal time-domain simulations. For the linear design, the turbine is modeled as

$$H_{\text{hydro}}(s) = 2\frac{z-s}{s+2z}\frac{1}{sT_y+1}, \quad z = \frac{1}{g_0 T_w} \quad (3)$$

where T_y is the servo time constant, g_0 the initial gate opening, and T_w the water time constant [23].

Following a gate opening, the pressure over the turbine falls before the water accelerates, due to the inertia in the water column. Because of this, the initial power surge will be in the opposite direction of the gate opening change. This behavior results in a bandwidth limitation, which in the linearized model (3) is characterized by the right half-plane (RHP) zero [23].

C. Battery Storage Model

In the time frame of interest for frequency control, the dynamics of battery storage units are dominated by the dynamics of the inverter and its controls [10], [11]. Assuming that the inverter dynamics have no significant impact on (1), see Remark 2, we therefore model batteries as ideal controllable power sources, with

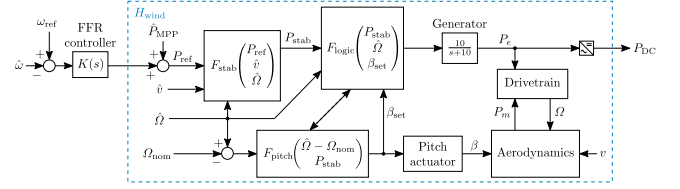$$H_{\text{battery}}(s) = 1.$$

Fig. 4. Block diagram of a variable-speed controlled WT [29].

For the simulation case study, we also keep track of the energy level to indicate the required battery size. Depending on the size of the energy storage, batteries can be used as both FCR and FFR. In this work, we consider that the storage is limited so that batteries are used only for FFR.

D. Wind Power Model

We consider a 8th-order WT model shown in Fig. 4. The model is based on the National Renewable Energy Laboratory (NREL) -MW baseline WT model [28]. The control system has been modified by adding a stabilizing feedback controller, F_{stab}, to allow the turbine to participate in FFR. For a full description and analysis of the modified turbine, the reader is referred to [29]. Here we give a brief overview of the WT model and its linearization.

The pitch controller, F_{pitch}, ensures that the rotor speed Ω does not exceed the rated speed Ω_{nom}, by adjusting the pitch angle β. The control logic, F_{logic} allows the turbine to operate in various operating modes by adjusting the generator set point and choosing when to activate the pitch controller.

Assume uncurtailed operation at the MPP below the rated wind speed, then $\beta = 0$ and the electric power output P_e is equal to the MPP power estimate $\hat{P}_{\text{MPP}}$. Assuming that the inverter dynamics have no significant impact on (1), we let $P_{\text{in}} = P_{\text{DC}} = P_e$. The mechanical power P_m is a function of rotor speed Ω and the wind speed v. Any deviation from the optimal speed Ω_{MPP} will result in a reduced sustainable power output. However, if operated below rated speed, the electric power can be temporarily increased, allowing the WT to participate in FFR. This, however, will decelerate the rotor and reduce the sustainable power output, as shown by the power/speed characteristics in Fig. 10(b). To ensure stability, a variable-speed feedback controller, F_{stab}, is implemented. The controller uses wind and rotor speed measurements $\hat{v}$ and $\hat{\Omega}$ to modify the power reference P_{ref} to P_{stab}. The turbine dynamics shown in Fig. 4 are ill-suited for linearization. However, if we set a minimum allowed rotor speed, then we can at least derive a linear worst-case representation of the turbine. As shown in [29], the dynamics most relevant for FFR are

$$P_e \approx \frac{s-z}{s+k_{\text{stab}}-z}P_{\text{ref}}$$

where the RHP zero z is a function of the drivetrain and aerodynamics, and k_{stab} is the effective stabilizing feedback gain from F_{stab} at the current wind speed. As the turbine decelerates, z increases. Keeping the turbine above the minimum allowed

speed, then $z \leq \bar{z}$. Let $k_{\text{stab}} = 2\bar{z}$, then

$$H_{\text{wind}}(s) = \frac{s - \bar{z}}{s + \bar{z}} \qquad (4)$$

is a linear representation useful for analysis and control design. If we let the minimum allowed speed be 80% of Ω_{MPP}, then $\bar{z} = 5.8v \times 10^{-3}$ [29].

Note that a 20% deceleration accounts for a larger absolute speed reduction at higher wind speeds, resulting in a larger allowable NMP zero bound, but the structure (4) will be the same at all wind speeds. As show in Section IV-C, the upper NMP zero bound is useful for robust coordination of FFR and FCR since (4) overestimates the decline in WT power output.

Remark 1: The linearized WT model (4) assumes operation at the MPP below the rated wind speed. The model implies that we cannot improve the energy output over time by increasing the output, since we are already operating at the MPP. Any temporary output increase will therefore have to be compensated by a reduced output in the future. We therefore expect that similar constraints will apply also when operating at the MPP above rated wind speed, if the converter is sized so that the electrical power can be increased above the mechanical rating of the WT.

III. DVPP CONTROL DESIGN

Using FFR from wind to assist FCR from slower conventional generation has been proposed in the literature [18]–[20]. In this work, we take this one step further. We develop a linear control design method that coordinates the dynamic response of a heterogeneous ensemble of plants, so that the combined Bode plot of all participating plants matches a target function over all frequency ranges. Using the target function (2) result is a DVPP that meets the SO's FCR-D requirements. The method is general and allows us to take into account energy capacity, power, and bandwidth limitations. Knowing the FCR-D requirements and the dimensioning fault, it is possible to account for saturation and ramp rate limits when choosing the DPFs. From a control design perspective, however, the dynamic limitations imposed by NMP zeros will be harder to address, since they also affect the phase and thus the stability margins. Dynamic limitations will always be relevant, regardless of the size of the disturbance. The main focus in this work is therefore on the combination of hydro and wind, both of which have NMP zero dynamics relevant for the FCR-D.

This section presents a coordinated FCR and FFR control design method. It can be applied globally, or locally in a DVPP. Our design is based on the COI model and assumes asymptotic synchronization on the average mode. In the end, stability is verified by applying the control and simulating the power system model.

A. Coordinated FCR and FFR Using Model-Matching

Let $D(s) = D$ represent the uncontrolled, proportional, frequency-dependent loads in the system and let $H_i(s)$ be the controllable power source, and $K_i(s)$ be the FCR controller at bus i. By breaking the loop at the input of the FCR controllers in Fig. 5, the *global* open-loop gain of the FCR control scheme
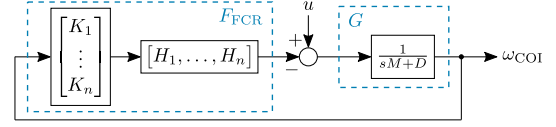

Fig. 5.   Block diagram of the FCR design problem.

becomes

$$L(s) = \sum_{i=1}^{n} L_i(s), \quad L_i(s) = G(s) \cdot H_i(s) \cdot K_i(s) \qquad (5)$$

where $G(s) = 1/(sM + D)$.

We pose the DVPP design as a decentralized model-matching problem. Let $L_{\text{des}}(s) = G(s) \cdot F_{\text{FCR}}(s)$ be the desired, stable, and MP loop-gain that fulfill the FCR-D specifications. The loop-gain of each plant is then given by

$$L_i(s) = c_i(s) \cdot L_{\text{des}}(s) = c_i(s) \cdot G(s) \cdot F_{\text{FCR}}(s) \qquad (6)$$

where $c_i(s)$ are DPFs to be designed. DPFs are frequency-dependent version of static participation factors [23], which allow us to take the dynamic characteristics of each device into account. The controller for subsystem i is then given by

$$K_i(s) = c_i(s) \cdot F_{\text{FCR}}(s)/H_i(s).$$

We say that perfect model-matching is achieved if

$$\sum_{i=1}^{n} c_i(s) = 1, \quad \forall s \in \mathbb{C} \qquad (7)$$

in which case $L_1(s) + \cdots + L_n(s) = c_1(s) \cdot L_{\text{des}}(s) + \cdots + c_n(s) \cdot L_{\text{des}}(s) = L_{\text{des}}(s)$. However, taking into account the dynamical constraints of the actuators $H_i(s)$, such as NMP zeros, we may have to relax (7) to ensure that $K_i(s)$ is proper and that the resulting closed-loop system is internally stable. We relax (7) by allowing a mismatch in the equality. Typically, we want a good match at steady state up to some frequency ω_B, e.g., we want $\sum_{i=1}^{n} c_i(j\omega) = 1$ for $\omega \in [0, \omega_B]$.

Remark 2: A rule of thumb is that, for the resulting closed-loop system to be close to nominal, we want a good match up until at least ten times the cross-over frequency [30]. For model-matching in the low-inertia N5 test case in Fig. 1(c), this indicates that $\omega_B \approx 2.6$ rad/s. This also justifies neglecting stable dynamics of batteries and power electronics in the FCR and FFR control design since these typically are $\gg 2.6$ rad/s [10], [11].

B. Internal Stability

In addition to shaping the COI frequency disturbance response, we have to ensure internal stability with respect to the interfaces between the plant $G(s)$, the FCR controllers $K_i(s)$, and the controllable power sources $H_i(s)$ in Fig. 5.

Theorem 1 ([31]): The system is internally stable if and only if the sensitivity
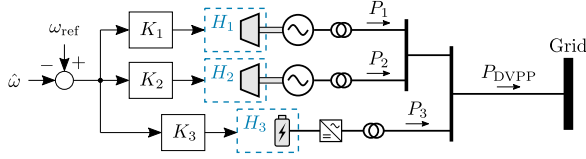
$$S(s) = \frac{1}{1 + L(s)} \qquad (8)$$

Fig. 6. One-line diagram of a battery–hydro DVPP.

is stable and no unstable pole-zero cancelations occur between plants and controllers $G(s)$, $H_i(s)$, and $K_i(s)$, $i \in \{1, \ldots, n\}$.

Corollary 1: In case of RHP poles $p_j \in \mathbb{C}_+$ in $H_i(s)$ or $G(s)$, we need that

$$L_i^{-1}(p_j) = 0.$$

Since we are not allowed to cancel RHP poles, any RHP poles must therefore remain in the global open-loop $L(s)$. However, if p_j belongs to $H_i(s)$, we may prestabilize $H_i(s)$ by first designing a local feedback controller [32].

Corollary 2: In the case of NMP zeros $z_j \in \mathbb{C}_+$ in $H_i(s)$ or $G(s)$, we need that

$$L_i(z_j) = 0.$$

Zeros cannot be moved by series compensation or feedback. Therefore, unlike unstable poles, these must remain in the system. However, since zeros are moved by parallel connections, as in Figs. 5 and 6, it is not necessary for the NMP zeros of $H_i(s)$ to remain in the global loop-gain $L(s)$.

For the remainder, we assume that $G(s)$ is stable and MP, and that any unstable poles in $H_i(s)$ have been prestabilized. The problem that remains is then how to deal with NMP zeros. Ideally, we want the global open-loop to be MP so that perfect matching (7) can be achieved.

C. Choosing Dynamic Participation Factors (DPFs)

There are many ways of choosing the DPFs $c_i(s)$, $i \in \{1, \ldots, n\}$. Ideally, the factors are distributed between VPP units to play on their dynamic strengths, compensate for their weaknesses, and align with economic considerations. To illustrate how this can be achieved, we here propose a method where the frequency control is divided up into slower FCR and faster FFR.

Let $c_i(s)$, $i \in \{1, \ldots, m\}$ and $c_i(s)$, $i \in \{m+1, \ldots, n\}$ be the DPFs for FCR and FFR, respectively. Let each producer specify a variable k_i indicating their willingness or marginal cost for supplying FCR and FFR. Normalize the constants so that $\sum_{i=1}^{m} k_i = 1$ and $\sum_{i=m+1}^{n} k_i = 1$.

Starting with FCR, let

$$c_i(s) = k_i \mathcal{B}_i(s) / \mathcal{B}_i(0), \quad i \in \{1, \ldots, m\}$$

where, as necessary according to Corollary 2,

$$\mathcal{B}_i(s) = \prod_{j=1}^{n_z} \frac{z_j - s}{s + p_j} \qquad (9)$$

contains all n_z NMP zeros of the plant $H_i(s)$. The poles p_j are design parameters, e.g., to adjust the cross-over frequency of

$L_i(s)$. A good starting point, however, is to let $p_j = z_j$ so that the DPFs are all-pass.

Next, we design the FFR participation factors. Let

$$c_i(s) = k_i \frac{\mathcal{B}_i(s)}{\mathcal{B}_i(\infty)} \left(1 - \sum_{l=1}^{m} c_l(s) \right), \quad i \in \{m+1, \ldots, n\}$$

where $\mathcal{B}_i(s)$ is the product (9). Note that $\mathcal{B}_i(\infty)$ is a negative real number if n_z is odd.

At this point, we have FCR and FFR controllers that achieve perfect matching $\sum_{i=1}^{n} c_i(s) = 1$ for $s = 0$ and $s \to \infty$. Since no NMP zeros are canceled, internal stability is achieved if the sensitivity (8) is stable. However, if any of the FFR plants $H_i(s)$ are NMP, we do not have perfect model-matching, due to the required modifier $\mathcal{B}_i(s)/\mathcal{B}_i(\infty)$. If the total sum is MP, however, this can be amended by adding a final normalization step $c_i'(s) = c_i(s)/\sum_{i=1}^{n} c_i(s)$.

IV. ILLUSTRATIVE EXAMPLES ON DVPP CONTROL DESIGN

In this section, we will show how a set of heterogeneous plants can be controlled so that they together form a DVPP with favorable MP characteristics. We do this, using DPFs as described in Section III. For simplicity, we consider open-loop control of a subsystem connected to the grid. Therefore, it is not yet possible to state any requirement on the loop gains (5) and (6). Instead, the design is specified in terms of the ideal FCR response (2). The insight gained from this will later be used for the Nordic case study.

A. FCR Provided by Two Hydrounits

Consider a subsystem with two 50-MVA hydrounits exporting power to the grid as shown in Fig. 6. Assume water time constants $T_{w,1} = 1.25$ s and $T_{w,2} = 2.5$ s, respectively, and an initial gate opening $g_0 = 0.8$ and servo time constant $T_y = 0.2$ s for both turbines, then

$$H_1(s) = 2 \frac{-s+1}{s+2} \frac{1}{s\,0.2+1}, \quad H_2(s) = 2 \frac{-s+0.5}{s+1} \frac{1}{s\,0.2+1}.$$

Goal: Design FCR controllers $K_1(s)$ and $K_2(s)$ for the two-hydro subsystem so that both units increase their steady-power output by 10 MW following 1-Hz frequency reference step, and so that $H_1(s) \cdot K_1(s) + H_2(s) \cdot K_2(s)$ comes close to the ideal FCR response (2) with $R_{FCR} = 20$ MW/Hz.

Solution: From Proposition 1 in Appendix B, we know that the two-hydro subsystem will have a RHP zero $z \in [0.5, 1]$. Thus, perfect matching is not realizable. The design criteria require that $c_1(0) = c_2(0) = 0.5$, and for internal stability, RHP zeros need to be included. Let $K_i(s) = c_i(s) \cdot F_{FCR}(s)/H_i(s)$, $i \in \{1, 2\}$ with

$$c_1(s) = 0.5 \frac{-s+1}{s+1} \quad \text{and} \quad c_2(s) = 0.5 \frac{-s+0.5}{s+0.5}. \qquad (10)$$

Result: The resulting sum equals

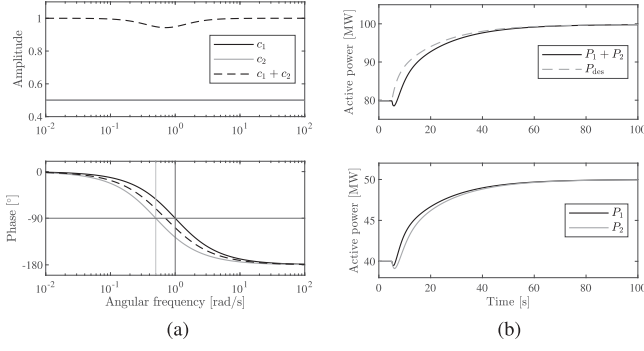$$c_1(s) + c_2(s) = \frac{(-s+1/\sqrt{2})(s+1/\sqrt{2})}{(s+1)(s+0.5)}.$$

Fig. 7. Power output and Bode diagram of the two hydrounits. (a) Participation factors. (b) Power injections.

Fig. 8. Bode diagram of participation factors, where $c(s) = \sum_{i=1}^{n} c_i(s)$. (a) Battery–hydro DVPP. (b) Wind–hydro DVPP.

Fig. 9. Power output of the battery–hydro DVPP. (a) Power injections. (b) Battery storage

As shown in Fig. 7(a), the model-matching is fulfilled at steady state with $c_1(0) + c_2(0) = 1$. However, the consequence of the RHP zero is that the DPF $c_1(s) + c_2(s)$ has a $-180°$ phase-shift at higher frequencies. The 1-Hz step response in Fig. 7(b) shows the characteristic NMP initial drop. This is an unavoidable physical property of the hydro governors that makes it impossible to fulfill the design target (2).

Although perfect matching is impossible, the performance can be improved by modifying the participation factors, e.g., by selecting faster poles in (10), or by selecting a design target (2) with a higher cross-over frequency. However, in low-inertia power systems, this may result in dangerously low closed-loop stability margins or even instability [21]. A more robust solution is to complement hydropower with FFR.

B. Battery Storage FFR Support

As shown in Section IV-A, it is impossible to achieve a MP FCR response using only hydrounits. To improve the transient response, one solution is to assist the hydrounits with FFR from a battery storage, forming a DVPP as shown in Fig. 6.

Goal: Consider the battery storage as an ideal controllable power source, with $H_3(s) = 1$. Design $K_3(s)$ so that the DVPP, with $K_i(s) = c_i(s) \cdot F_{\text{FCR}}(s)/H_i(s)$, fulfills

$$\sum_{i=1}^{3} K_i(s) \cdot H_i(s) = F_{\text{FCR}}(s) \qquad (11)$$

that is, design the DPFs as in (7).

Solution: From Proposition 2 in Appendix B, we know that since $\text{Re}[c_1(j\omega) + c_2(j\omega)] \leq 0 \ \forall \omega$, the complementary DPF

$$c_3(s) = 1 - (c_1(s) + c_2(s)) = 2s\frac{(s + 0.75)}{(s + 1)(s + 0.5)}$$

is guaranteed to be stable and MP. With the battery dynamics, $H_3(s)$, being stable and MP, perfect matching is achieved with $K_3(s) = c_3(s) \cdot F_{\text{FCR}}(s)/H_3(s)$.

Result: As seen in Fig. 8(a), the battery compensates for the phase lag of the hydrounits so that $\sum_{i=1}^{n} c_i(s) = 1$. As a result, the DVPP output in Fig. 9(a) matches the ideal response
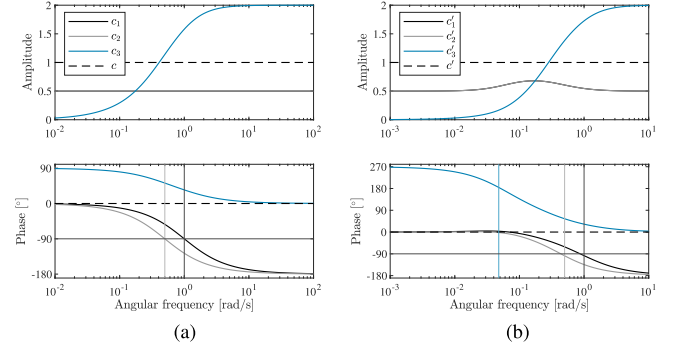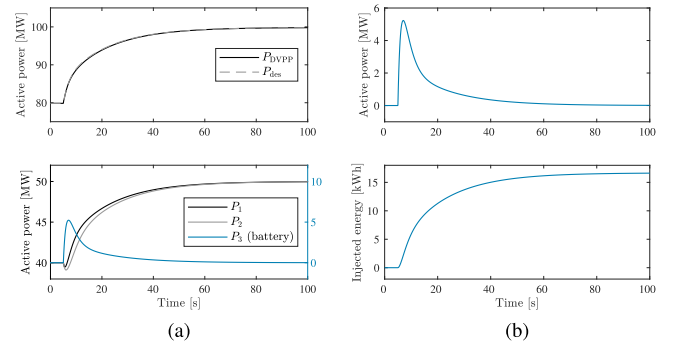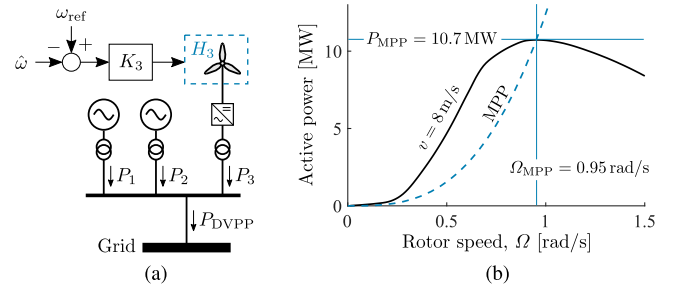

Fig. 10. Wind–hydro DVPP with a 30 MW wind farm. (a) One-line diagram of the DVPP. (b) Wind farm power/speed characteristic.

$P_{\text{des}} = F_{\text{FCR}}(s)(\omega_{\text{ref}} - \hat{\omega})$. With a more detailed battery plus converter model, perfect matching can only be expected up to a certain frequency.

Having a stable MP controllable power source is ideal for providing FFR in a DVPP. With a battery storage, bounds on achievable performance are determined by the power rating and the energy storage capacity. As shown in Fig. 9(b), we need a battery–converter rating of at least 5.5 MW and at least 17 kWh energy storage capacity for assisting in the step response.
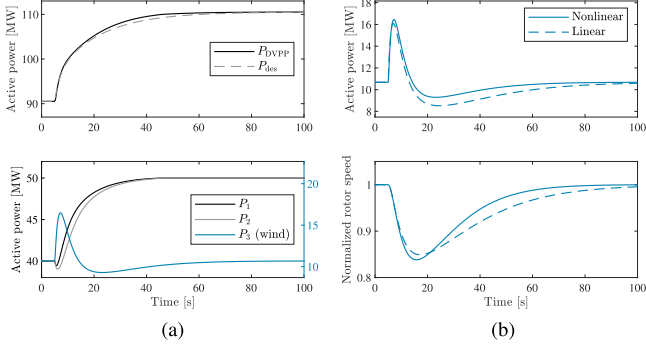
Fig. 11. Power output of the wind–hydro DVPP. (a) Power injections. (b) WT response.

C. Wind Power FFR Support

An alternative to providing FFR with battery storage is to assist with FFR from wind power. Compared with the battery solution, however, for the WT, its dynamics cannot be neglected. Here, we consider WTs operated at the MPP, but below the rated wind speed so that the power output can, at least temporarily, be increased. When commanded by the FFR controller to exert power above the MPP, the rotor decelerates, and thus the sustainable power output decreases, as shown by the power/speed characteristics in Fig. 10(b). The decline in sustainable power manifests in an NMP behavior [29].

Goal: Consider a 30-MW wind park connected to the subsystem as shown in Fig. 10. Assume initially that $P_3 = P_{\mathrm{MPP}}$. Let the wind speed be $v = 8$ m/s. Then, the all-pass filter

$$H_3(s) = \frac{s - 0.048}{s + 0.048} \qquad (12)$$

is a suitable linear representation of the WT dynamics [29]. Design $K_3(s)$ so that the DVPP fulfills (11).

Solution: Using the three-step approach in Section III-C, let $c_1(s)$ and $c_2(s)$, as in (10), and $c_3(s) = (1 - c_1(s) - c_2(s))H_3(s)$. The normalized DPFs $c_i'(s) = c_i(s)/\sum_{i=1}^{3} c_i(s)$ then give perfect model-matching with $\sum_{i=1}^{3} c_i'(s) = 1$.

Result: As seen in the Bode diagram Fig. 8(b), the wind farm compensates for the phase lag of the hydrounits at higher frequencies. From Proposition 3 in Appendix B, we know that that perfect matching can always be achieved, provided that we allow for interaction between the FCR and FFR controllers. For example, in order to achieve $\sum_{i=1}^{3} c_i'(j\omega) = 1$ for low frequencies where $\mathrm{Re}[c_3'(j\omega)] < 0$, then we need the hydrounits to compensate with excessive FCR, i.e., $\mathrm{Re}[c_1'(j\omega) + c_2'(j\omega)] > 1$. This is seen in Fig. 8(b), where the normalization step increases the gain of the hydrounits at $\omega \approx 0.1$ rad/s. A larger separation between the zeros gives less interaction between the competing NMP dynamics.

The coordinated response to a 1-Hz reference step is shown in Fig. 11(a). The small discrepancy between the actual DVPP response and the ideal response comes from the fact that the linear model (12) underestimates the power output of the nonlinear WT dynamics [29], as seen in Fig. 11(b).

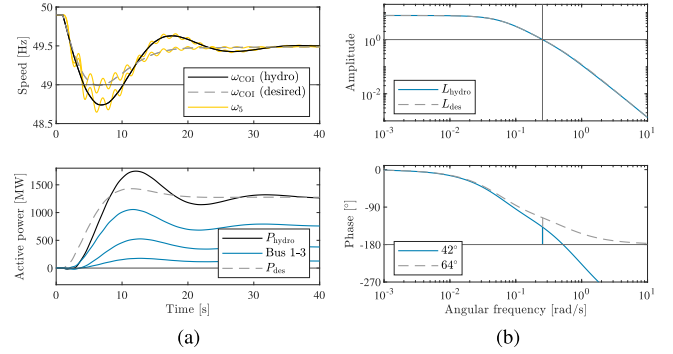| Bus	FCR (%)	T_y	T_w	g_0
1	60	0.2	0.7	0.8
2	30	0.2	1.4	0.8
3	10	0.2	1.4	0.8

Fig. 12. N5 test system with hydro-FCR. (a) FCR response to a 1400-MW fault. (b) Bode diagram.

V. COORDINATED FCR AND FFR IN THE N5 TEST SYSTEM

In this section, we study FCR and FFR control designs in the N5 test system introduced in Section II-A. First we show that, providing FCR solemnly from hydro power, the MP design target (2) cannot be achieved. Then, we show that the desired MP design can be achieved by combining hydro and wind. Finally, we compare the performance of the coordinated FCR and FFR design via DVPP to a system that uses conventional PI/droop hydro governors and discontinuous wind-FFR.

A. Coordinated Wind and Hydropower in the N5 Test System

Consider the N5 110 GWs test case studied in Section II-A, but now assume that the FCR is provided by hydrounits. Based on the test case in [24], let parameters and FCR resources be distributed according to Table II. The FCR controllers for the three hydrounits are designed following the same procedure as in Section IV-A. By design, the target (2) just barely fulfills the FCR-D requirements with ideal actuation and control $P_{\mathrm{des}} = F_{\mathrm{FCR}}(s)(\omega_{\mathrm{ref}} - \hat{\omega})$. Since the hydro-FCR is NMP, the FCR-D requirements are no longer fulfilled since the combined output at buses 1, 2, and 3, $P_{\mathrm{hydro}} \neq P_{\mathrm{des}}$, as seen in Fig. 12(a). The reason for this is the negative phase-shift, in the aggregated hydro open-loop $L_{\mathrm{hydro}}(s)$ resulting from the NMP zero, shown in Fig. 12(b).

Now let the hydro resources be complemented with FFR from wind power at buses 2 and 4, as shown in Fig. 1(a). Assume that the WTs participating in FFR have a total nominal power rating of 2000 MW distributed according to Table III. Using the same design procedure described in Section IV-C, we leverage the FFR capability of the WTs to achieve perfect matching. With a total output P_{wind}, the combined wind–hydro-FCR and FFR response closely matches the ideal response P_{des}, as seen in Fig. 13(a). As

WT NOMINAL POWER RATING P_{NOM}, WIND SPEEDS v, PREFAULT POWER INJECTIONS P_{MPP}, AND FFR DISTRIBUTION

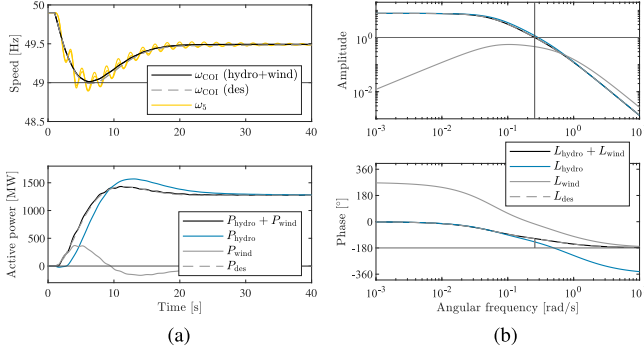| Bus	P_{nom} (MW)	v (m/s)	P_{MPP} (MW)	FFR (%)
2	500	10	348	33
4	1500	8	534	67

Fig. 13. N5 test system with coordinated FCR and FFR. (a) Response to a 1400-MW fault. (b) Bode diagram.
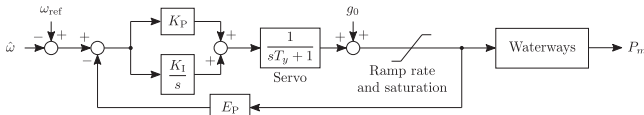

Fig. 14. Block diagram of the hydroturbine with a PI/droop governor.

shown in Fig. 13(b), with the aggregate wind open-loop $L_{\text{wind}}(s)$, the FCR-D requirements are now fulfilled with no significant change to the cross-over frequency of $L_{\text{hydro}}(s)$.

Comparing the disturbance response in Fig. 13(a) with Fig. 12(a), we see that the desired FCR-D response is met by adding just enough input power from the WTs. By matching the desired FCR-D response both in strength and response speed, we meet the requirements without unnecessary overdimensioning of the FFR. The DVPP design fulfills the requirements without increasing the response speed of existing hydrounits and without the need to add extra battery storage. The steady FCR response is the same in Figs. 12(a) and 13(a) since it is provided solemnly by hydro in both scenarios. However, the overshoot and therefore the maximum power output of the hydrounits are reduced with assistance from the WTs.

B. Conventional Wind and Hydro Control in the N5 Test System

Let us compare the coordinated FCR and FFR design to a more conventional FCR and FFR control scheme. We let the hydrounits at buses 1, 2, and 3 use conventional PI/droop governors, as shown in Fig. 14. Based on the FCR-D requirements, all PI controllers have their proportional gain and integral gain set to $K_P = 1.2$ p.u and $K_I = 0.6$ p.u./s, respectively. The droop gains E_P are chosen so that the FCR are allocated according to Table II, as in the previous case study.
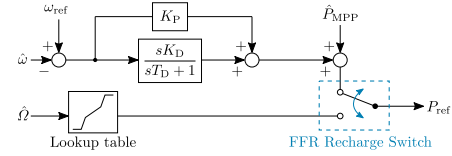

Fig. 15. Block diagram of the WT power controller with proportional-derivative FFR control and MPP tracking capability. The controller can switch between the two modes to recharge the WT following a frequency event.
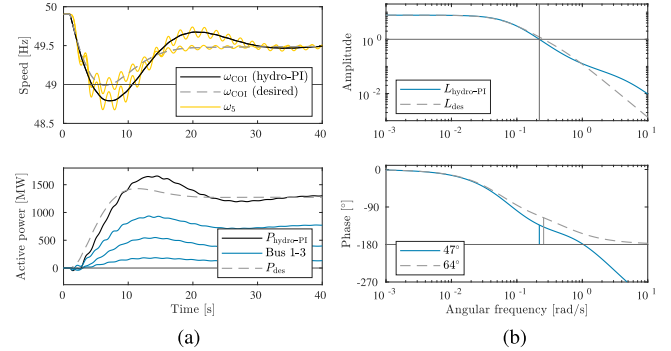

Fig. 16. N5 test system with conventional PI/droop hydro-FCR. (a) FCR response to a 1400-MW fault. (b) Bode diagram.

The NMP hydroturbines have a delayed activation time, as we see in both Figs. 12(a) and 16(a). To match the transient performance of the MP design target (2), we therefore need to increase the response speed of the hydro-FCR, in order to catch up with the desired MP response. To meet the FCR-D requirements, we therefore need to allow for a higher ramp rate. This can be achieved by adjusting the proportional and integral gains and/or adding a derivative action. To get a faster response speed, we need to increase the open-loop gain at higher frequencies. Regardless of how cleverly we tune our controllers, however, a faster FCR response cannot be achieved without reducing the closed-loop stability margin of the system because of the NMP dynamics of the waterways. Hence, instead of trying to compensate for the NMP zero dynamics with faster hydro-FCR, we complement the hydro-FCR with FFR from wind.

One of the challenges with wind-FFR is to account for the reduced sustainable output that follows when deviating from the MPP. The most commonly proposed solution to this problem is to switch over from FFR to MPP tracking control. This recharges the FFR by drawing power from the grid, allowing the WT to return to the MPP [18], [19]. This is also the prevailing solution for providing FFR from other controllable but limited energy reservoirs, e.g., battery storage [14], [22].

Let the wind-FFR be implemented using PD controllers at buses 2 and 4, as shown in Fig. 15. We set the derivative time constants $T_D = 1$ s and derivative controller gains $K_D = 10K_P$ at both buses. The proportional gains K_P are then selected so that the FCR-D requirements are met, while allocating the FFR according to Table III, as in the previous case study. As can
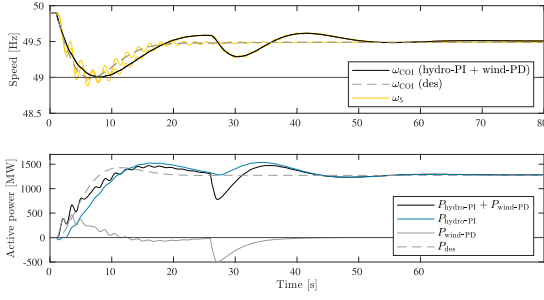
Fig. 17. N5 test system with conventional PI/droop hydro-FCR and discontinuous wind-FFR
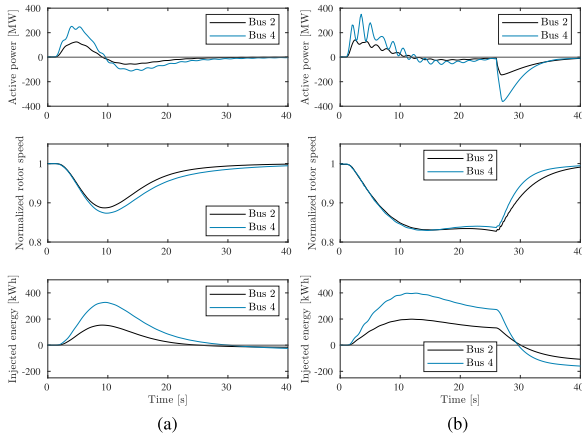

Fig. 18. A comparison between the two wind-FFR methods. (a) Continuous FFR in Fig. 13. (b) Discontinuous FFR in Fig. 17.

be seen in Fig. 17, the WTs inject power to the grid directly after the fault. This improves the transient frequency response so that the nadir is halted at 49.0 Hz, as desired. At 25 s after the fault, the WTs are switched over to MPP tracking control in order to restore the WT rotor speed, as shown in Fig. 18(b). This results in an undesired (albeit well-known and inevitable) second frequency drop, as seen in Fig. 17.

C. A Comparison Between the Control Methods

In Fig. 18, we compare the continuous wind-FFR from Section V-A (based on coordinated DVPP design) to the discontinuous wind-FFR from Section V-B. Notice that the discontinuous wind-FFR is more oscillatory than the continuous wind-FFR. The reasons for this are twofold. First, comparing Figs. 12(a) and 16(a), we see that the PI/droop controlled hydropower destabilizes the interarea modes more than the hydro-FCR from the model-matching design in Section V-A. Consequently, we get larger frequency oscillations, which are in turn picked up by the fast WT controllers. Second, the discontinuous wind-FFR designed in Section V-B is more aggressive at higher frequencies. The result is a wind-FFR that not only compensates for the hydro-FCR but also improves the power oscillation damping compared to the desired MP response, as seen in Fig. 17.

If better power oscillation damping is desired in the model-matching design, this could of course be included in the design target (2).

As seen in Fig. 18, the discontinuous wind-FFR results in a larger WT rotor speed reduction. Depending on when the FFR recharge switch is activated, the discontinuous wind-FFR may also stay at low rotor speed, below the MPP, for a longer period of time. The net result is a larger loss of energy production by the WTs, compared to the continuous wind-FFR solution. To stabilize the grid at 49.5 Hz, this energy loss has to be met by the hydrounits. In the N5 test system example, the hydro-FCR needs to supply an extra 50 kWh to compensate for the continuous wind-FFR in Section V-A, whereas an extra 285 kWh is required to compensate for the discontinuous wind-FFR in Section V-B.

The proposed DVPP design method is aligned with the FFR market solution developed to cope with future low-inertia scenarios in the Nordic grid [22]. To address limitations caused by the NMP characteristics of hydro and wind, the proposed DVPP solution targets the whole angular frequency range, so that the interactions between slow and fast dynamics can be addressed when distributing frequency reserves. One advantage of the proposed model-matching procedure is that it combines FCR and FFR in a continuous linear feedback control law, as compared to solutions that rely on predefined feedforward switching protocols to disconnect or recharge unsustainable FFR resources [14], [18], [19], [22]. The drawback of feedforward methods is that we need more accurate models, since we do not use feedback to compensate for uncertainties and unexpected fault scenarios. However, even for the nominal N5 test case, the proposed DVPP design method outperforms the conventional FCR and FFR design. First, as seen in Fig. 17, the frequency overshoots when restoring the frequency. This is because there is no coordinating normalization step (see Section III-C) between the hydro-FCR and wind-FFR. Second, since the WT rotor speed is recovered without coordination with the hydro-FCR, there will be a second frequency dip. Finally, the discontinuous wind-FFR is designed so that we have a buffer period between FFR deployment and rotor speed recovery, in accordance to [22]. This means that the WTs stay for a longer time outside of the MPP. As a result, the discontinuous wind-FFR is more expensive when it comes to energy usage, as seen in Fig. 18.

Tuning the conventional PI/droop governors is difficult since the open-loop system is not linear in the control parameters K_P, K_I, and E_P. For the discontinuous FFR, we get an extra layer of complexity since we have to account for different recharge timings. With a heterogeneous ensemble of controllable devices, the conventional design method gives us all the prerequisites for a challenging optimization problem. With the proposed DVPP design, we circumvent most of this problem. The only real design choice is to tune the ideal linear design target (2). The tuning method used in this article is described in Appendix A. The rest of the controller design then follows the algorithm laid out in Section III-C.

VI. CONCLUSION

In this article, a method for distributing ancillary FCR services between a heterogeneous ensemble of controllable plants, by forming a DVPP, has been derived. The method matches the aggregated loop-gain of all participating devices to the Bode diagram of a target function, specified by the SO's requirements. Treating the design as a decentralized model-matching problem, the final controller can be implemented with local frequency measurements. The proposed DVPP design was implemented in a model of the Nordic synchronous grid. By compensating for the NMP dynamics of hydro, the FCR-D requirements were fulfilled with quite moderate wind resources, without the need for curtailment or battery installations.

Some limitations of our approach are the neglect of ramp rate and saturation limits in the design. These are only indirectly addressed when choosing the DPFs. This is to be addressed in future work. Another limitation is the use of the COI model (1) in the analysis. This is a common modeling assumption used both in the industry and in academia. The modeling choice is further justified since there is no automatic control of the tie-line power flows, or area control error, in the Nordic grid [24]. Instead, area control errors are treated indirectly when allocating FCR reserves. Modeling the grid as a single machine, however, means that we cannot model the voltage dynamics of loads, since this would require a model of the network. This leaves out actuators that could otherwise be exploited in the FCR and FFR design. For instance, it can be shown that power system stabilizers in combination with voltage-dependent loads can improve the nadir. As part of our future and ongoing work, the analysis is extended to include reactive power and voltage control [33]. The DVPP design is also extended to account for device-level constraints, uncertainty, and real-time adaption of DPFs.

In low-inertia power systems, it is relevant to consider how fast-acting FCR affects higher order network dynamics, such as the stability of interarea oscillations. Our preliminary results show how the analysis can be extended to include decentralized stability guarantees when committing new devices to the FCR and the FFR [34]. Future work will also address saturation constrains, more detailed models, and minimum energy control (to avoid overdimensioning).

APPENDIX

A. Design of FCR-D Design Target

The FCR-D design target (2) is tuned to match the SO's requirements. Following an immediate frequency fall from 49.9 to 49.5 Hz, the reserves should be 50% activated within 5 s [26]. This can be met by the first-order design target

$$F_{\text{temp}}(s) = R_{\text{FCR}} \frac{1}{sT_{\text{temp}} + 1} \tag{13}$$

with the time constant

$$T_{\text{temp}} = -5/\ln(0.50) \approx 7.2. \tag{14}$$

Considering a 1400-MW dimensioning fault and 400-MW/Hz inherent load damping, we let the gain

$$R_{\text{FCR}} = 1400/(49.9 - 49.5) - 400 = 3100$$

so that the frequency stabilizes at 49.5 Hz. The frequency disturbance response, combining (1) with (13),

$$\frac{1}{sM + 400 + F_{\text{temp}}(s)} \tag{15}$$

fulfills the FCR-D requirements. With $W_{\text{kin}} = 110$ GWs, the nadir reaches almost 49.0 Hz following a 1400-MW load step. The first-order design target (13) will, however, unavoidably lead to an overshoot and ensuing oscillations when restoring the system frequency. This is amended by adding a lead-filter to (13) and readjusting the time constant (14) so that the disturbance response (15) still reaches a nadir of 49.0 Hz. This does not significantly change the FCR activation time, but gives a more desirable dynamic response. For the N5 test system, the second-order transfer function (2) is a suitable design target, as shown in Fig. 1(b).

B. Conditions for Perfect Model-Matching With NMP Plants

Proposition 1: Consider two stable plants $c_i(s)$, $i \in \{1, 2\}$ with one real NMP zero each at $z_i > 0$. Assume positive signed dc gain, i.e., let $c_i(0) > 0$. Then, $c(s) = c_1(s) + c_2(s)$ must have at least one real NMP zero $z \in [z_1, z_2]$.

Proof: Let $c_i(s) = a_i(s)(z_i - s)/b_i(s)$, where $b_i(s)$ and $a_i(s)$ are polynomials with no RHP roots. Without loss of generality, assume that plants have been normalized so that $b_1(s) = b_2(s) = b(s)$. Then, $c(s) = c_1(s) + c_2(s)$ is

$$c(s) = (z_1 a_1(s) + z_2 a_2(s) - s(a_1(s) + a_2(s))) \Big/ b(s)$$

and has zeros on the positive real axis where

$$\frac{z_1 a_1(\sigma) + z_2 a_2(\sigma)}{a_1(\sigma) + a_2(\sigma)} - \sigma = 0, \quad \sigma \geq 0. \tag{16}$$

With $c_i(0) > 0$, and with no zeros in the RHP, $a_i(\sigma) > 0$ $\forall \sigma \geq 0$. The first term in (16) is therefore a convex combination

$$\frac{z_1 a_1(\sigma) + z_2 a_2(\sigma)}{a_1(\sigma) + a_2(\sigma)} \in [z_1, z_2] \quad \forall \sigma \geq 0.$$

Since $0 < \min(z_1, z_2) \leq \max(z_1, z_2) < \infty$, (16) must have at least one real NMP zero, where $\sigma = z \in [z_1, z_2]$. ∎

Proposition 2: Consider a stable and proper plant $c_1(s)$. If $\text{Re}[c_1(j\omega)] \leq 1 \forall \omega$, then perfect matching is achieved with the stable and MP plant $c_2(s) = 1 - c_1(s)$.

Proof: If $c_1(s)$ is stable and proper, then so is $c_2(s) = 1 - c_1(s)$. If $\text{Re}[c_1(j\omega)] \leq 1 \ \forall \omega$, then $\text{Re}[c_2(j\omega)] \geq 0 \ \forall \omega$. Since $c_2(s)$ is stable and positive real, it is also MP [35]. ∎

Proposition 3: Consider a stable first-order plant

$$c_1(s) = (1 + \varepsilon) \frac{z_1 - s}{s + z_1}$$

with RHP zero $z_1 > 0$ and $\varepsilon > 0$ so that $c_1(0) > 1$. Then, under perfect matching, the assisting first-order plant $c_2(s) =$

$1 - c_1(s)$ is stable, has a RHP zero in $z_2 = z_1 \varepsilon/(2 + \varepsilon)$, and has a negative steady-gain $c_2(0) = -\varepsilon < 0$.

Proof: The assisting plant $c_2(s)$ is

$$1 - c_1(s) = \frac{s(2 + \varepsilon) - z_1 \varepsilon}{s + z_1} = \frac{2 + \varepsilon}{s + z_1}\left(s - \frac{z_1 \varepsilon}{2 + \varepsilon}\right). \quad \blacksquare$$

REFERENCES

[1] E. Dall'Anese, S. S. Guggilam, A. Simonetto, Y. C. Chen, and S. V. Dhople, "Optimal regulation of virtual power plants," *IEEE Trans. Power Syst.*, vol. 33, no. 2, pp. 1868–1881, Mar. 2018.

[2] F. Milano, F. Dörfler, G. Hug, D. J. Hill, and G. Verbič, "Foundations and challenges of low-inertia systems (invited paper)," in *Proc. Power Syst. Comput. Conf.*, 2018, pp. 1–25.

[3] K. M. J. Rahman, M. M. Munnee, and S. Khan, "Largest blackouts around the world: Trends and data analyses," in *Proc. IEEE Int. WIE Conf. Elect. Comput. Eng.*, 2016, pp. 155–159.

[4] R. Bründlinger, "Review and assessment of latest grid code developments in Europe and selected international markets with respect to high penetration PV," in *Proc. 6th Sol. Integration Workshop*, 2016, pp. 14–17.

[5] H. Saboori, M. Mohammadi, and R. Taghe, "Virtual power plant (VPP), definition, concept, components and types," in *Proc. Asia-Pacific Power Energy Eng. Conf.*, 2011, pp. 1–4.

[6] S. Ghavidel, L. Li, J. Aghaei, T. Yu, and J. Zhu, "A review on the virtual power plant: Components and operation systems," in *Proc. IEEE Int. Conf. Power Syst. Technol.*, 2016, pp. 1–6.

[7] M. Vasirani, R. Kota, R. L. G. Cavalcante, S. Ossowski, and N. R. Jennings, "An agent-based approach to virtual power plants of wind power generators and electric vehicles," *IEEE Trans. Smart Grid*, vol. 4, no. 3, pp. 1314–1322, Sep. 2013.

[8] M. Alvarez, S. K. Rünnberg, J. Bermúdez, J. Zhong, and M. H. J. Bollen, "A generic storage model based on a future cost piecewise-linear approximation," *IEEE Trans. Smart Grid*, vol. 10, no. 1, pp. 878–888, Jan. 2019.

[9] P. Moutis, P. S. Georgilakis, and N. D. Hatziargyriou, "Voltage regulation support along a distribution line by a virtual power plant based on a center of mass load modeling," *IEEE Trans. Smart Grid*, vol. 9, no. 4, pp. 3029–3038, Jul. 2018.

[10] H. H. Alhelou, P. Siano, M. Tipaldi, R. Iervolino, and F. Mahfoud, "Primary frequency response improvement in interconnected power systems using electric vehicle virtual power plants," *World Elect. Veh. J.*, vol. 11, no. 2, pp. 1–13, May 2020.

[11] J. Schiffer, D. Goldin, J. Raisch, and T. Sezi, "Synchronization of droop-controlled microgrids with distributed rotational and electronic generation," in *Proc. IEEE 52nd Conf. Decis. Control*, 2013, pp. 2334–2339.

[12] W. Zhong, J. Chen, M. Liu, M. A. A. Murad, and F. Milano, "Coordinated control of virtual power plants to improve power system short-term dynamics," *Energies*, vol. 14, no. 4, Feb. 2021, Art. no. 1182.

[13] "POSYTYF. POSYTYF project: Powering system flexibility in the future through renewable energy sources," Accessed: Jun. 23, 2022. [Online]. Available: https://posytyf-h2020.eu/

[14] J. Melki and H. Ghasemi, "Investigation of frequency containment reserves with inertial response and batteries," Bachelor's Thesis, KTH Royal Institute of Technology, Stockholm, 2019.

[15] F. L. Müller and B. Jansen, "Large-scale demonstration of precise demand response provided by residential heat pumps," *Appl. Energy*, vol. 239, pp. 836–845, Apr. 2019.

[16] W. Li and G. Joos, "A power electronic interface for a battery supercapacitor hybrid energy storage system for wind applications," in *Proc. IEEE Power Electron. Specialists Conf.*, 2008, pp. 1762–1768.

[17] M. E. Glavin, P. K. W. Chan, S. Armstrong, and W. G. Hurley, "A standalone photovoltaic supercapacitor battery hybrid energy storage system," in *Proc. 13th Int. Power Electron. Motion Control Conf.*, 2008, pp. 1688–1695.

[18] J. Morren, S. W. H. de Haan, W. L. Kling, and J. A. Ferreira, "Wind turbines emulating inertia and supporting primary frequency control," *IEEE Trans. Power Syst.*, vol. 21, no. 1, pp. 433–434, Feb. 2006.

[19] X. Zhao, Y. Xue, and X.-P. Zhang, "Fast frequency support from wind turbine systems by arresting frequency nadir close to settling frequency," *IEEE Open Access J. Power Energy*, vol. 7, pp. 191–202, 2020.

[20] F. Wilches-Bernal, J. H. Chow, and J. J. Sanchez-Gasca, "A fundamental study of applying wind turbines for power system frequency control," *IEEE Trans. Power Syst.*, vol. 31, no. 2, pp. 1496–1505, Mar. 2016.

[21] E. Agneholm *et al.*, "FCR-D design of requirements phase 2," ENTSO-E, Tech. Rep., 2019, [Online]. Available: https://www.statnett.no/globalassets/for-aktorer-i-kraftsystemet/utvikling-av-kraftsystemet/nordisk-frekvensstabilitet/fcr-d-design-of-requirements--phase-2.pdf

[22] ENTSO-E, "Fast frequency reserve solution to the Nordic inertia challenge," Tech. Rep., 2019, [Online]. Available: https://www.statnett.no/globalassets/for-aktorer-i-kraftsystemet/utvikling-av-kraftsystemet/nordisk-frekvensstabilitet/ffr-stakeholder-report_13122019.pdf

[23] P. Kundur, *Power System Stability and Control*. New York, NY, USA: McGraw-Hill, 1994.

[24] L. Saarinen, P. Norrlund, U. Lundin, E. Agneholm, and A. Westberg, "Full-scale test and modelling of the frequency control dynamics of the nordic power system," in *Proc. IEEE Power Energy Soc. Gen. Meeting*, 2016, pp. 1–5.

[25] H. Québec and The MathWorks, "Simscape electrical reference (specialized power systems)," Natick, MA, USA, Tech. Rep., 2020.

[26] A. Haider, "Nordic synchronous area proposal for additional properties of FCR in accordance with Article 154(2) of the Commission Regulation (EU) 2017/1485 of 2 August 2017 establishing a guideline on electricity transmission system operation," ENTSO-E, 2018.

[27] Statnett NordLink, Accessed: Jun. 23, 2022. [Online]. Available: https://www.statnett.no/en/our-projects/interconnectors/nordlink/

[28] J. Jonkman, S. Butterfield, W. Musial, and G. Scott, "Definition of a 5-MW reference wind turbine for offshore system development," NREL, USA, Tech. Rep. NREL/TP-500-38060, 2009.

[29] J. Björk, D. V. Pombo, and K. H. Johansson, "Variable-speed wind turbine control designed for coordinated fast frequency reserves," *IEEE Trans. Power Syst.*, vol. 37, no. 2, pp. 1471–1481, Mar. 2022.

[30] S. Skogestad and I. Postlethwaite, *Multivariable Feedback Control: Analysis and Design*, 2nd ed. Hoboken, NJ, USA: Wiley, 2007.

[31] K. Zhou, *Robust and Optimal Control*. Englewood Cliffs, NJ, USA: Prentice-Hall, 1996.

[32] R. Pates and E. Mallada, "Robust scale-free synthesis for frequency control in power systems," *IEEE Trans. Control Netw. Syst.*, vol. 6, no. 3, pp. 1174–1184, Sep. 2019.

[33] V. Häberle, M. W. Fisher, E. Prieto-Araujo, and F. Dörfler, "Control design of dynamic virtual power plants: An adaptive divide-and-conquer approach," *IEEE Trans. Power Syst.*, early access, Dec.. 31, 2021, doi: 10.1109/TPWRS.2021.3139775.

[34] J. Björk, "Fundamental control performance limitations for interarea oscillation damping and frequency stability," Ph.D. dissertation, KTH Royal Institute of Technology, Stockholm, 2021.

[35] P. Ioannou and G. Tao, "Frequency domain conditions for strictly positive real functions," *IEEE Trans. Autom. Control*, vol. AC-32, no. 1, pp. 53–54, Jan. 1987.

Joakim Björk (Member, IEEE) received the M.Sc. degree in energy systems engineering from Uppsala University, Uppsala, Sweden, in collaboration with the Swedish University of Agricultural Sciences, Uppsala, Sweden, in 2016, and the Ph.D. degree in electrical engineering from the Division of Decision and Control Systems, KTH Royal Institute of Technology, Stockholm, Sweden, in 2021.

Since 2021, he has been with Department of Power Systems, Swedish national grid, Sundbyberg, Sweden. His research interests include fundamental control limitations in networked control systems with applications in frequency and voltage control of ac–dc power systems.

Karl Henrik Johansson (Fellow, IEEE) received the M.Sc. degree in electrical engineering and the Ph.D. degree in automatic control from Lund University, Lund, Sweden.

He is currently a Professor with the School of Electrical Engineering and Computer Science, KTH Royal Institute of Technology, Stockholm, Sweden, and the Director of Digital Futures, Stockholm. He has held visiting positions with UC Berkeley, Caltech, NTU, HKUST Institute of Advanced Studies, and NTNU. His research interests include networked control systems and cyber-physical systems with applications in transportation, energy, and automation networks.

Dr. Johansson is the President of the European Control Association and member of the IFAC Council, and was on the IEEE Control Systems Society Board of Governors and the Swedish Scientific Council for Natural Sciences and Engineering Sciences. He has received several Best Paper Awards and other distinctions from IEEE, IFAC, and ACM. He was a Wallenberg Scholar with the Knut and Alice Wallenberg Foundation. He has received Swedish Research Council Distinguished Professor, Future Research Leader Award from the Swedish Foundation for Strategic Research, the triennial IFAC Young Author Prize, and IEEE Control Systems Society Distinguished Lecturer. He is a Fellow of the Royal Swedish Academy of Engineering Sciences.

Florian Dörfler (Senior Member, IEEE) received the Diploma degree in engineering cybernetics from the University of Stuttgart, Stuttgart, Germany, in 2008, and the Ph.D. degree in mechanical engineering from the University of California, Santa Barbara, CA, USA, in 2013.

He is currently an Associate Professor with the Automatic Control Laboratory, and the Associate Head of the Department of Information Technology and Electrical Engineering, ETH Zurich, Zurich, Switzerland. From 2013 to 2014, he was an Assistant Professor with the University of California Los Angeles. His research interests include control, optimization, and system theory with applications in network systems, especially electric power grids.

Dr. Dörfler is the recipient of the Distinguished Young Research Awards by IFAC (Manfred Thoma Medal 2020) and EUCA (European Control Award 2020), the 2010 ACC Student Best Paper Award, the 2011 O. Hugo Schuck Best Paper Award, the 2012–2014 Automatica Best Paper Award, the 2016 IEEE Circuits and Systems Guillemin-Cauer Best Paper Award, and the 2015 UCSB ME Best Ph.D. Award. His students were winners or finalists for Best Student Paper Awards at the European Control Conference (2013, 2019), the American Control Conference (2016), the Conference on Decision and Control (2020), the PES General Meeting (2020), the PES PowerTech Conference (2017), and the International Conference on Intelligent Transportation Systems (2021).